This manuscript is a postprint of an article that has finally been published as:
Erlind Mysliu, Otto Lunder, Andreas Erbe: Role of aluminium hydrides in localised corrosion of aluminium revealed by operando Raman spectroscopy, *Physical Chemistry Chemical Physics*, **25**, 11845-11857 (**2023**). DOI: 10.1039/D3CP00522D

Final published version of the manuscript is available from:
https://doi.org/10.1039/D3CP00522D

Modifications compared to the accepted manuscript:
- The link to the associated research data (ref. 61) has been updated with the correct, final link which is the same as in the published version
- The image in Figure 1 has been removed due to unresolved copyright issues for self-archiving purposes; the link to the original source is included

Journal Name

ARTICLE TYPE

Cite this: DOI: 00.0000/xxxxxxxxxx

Role of aluminium hydrides in localised corrosion of aluminium revealed by operando Raman spectroscopy†

Erlind Mysliu,[a] Otto Lunder,[b] and Andreas Erbe*[a]

Received Date
Accepted Date

DOI: 00.0000/xxxxxxxxxx

Filiform corrosion (FFC) is characteristic of metals such as aluminium and magnesium, usually takes place on coated metals, and spreads from coating defects in the form of filaments with a width on the order of 100 µm. In this work, in situ and operando Raman spectroscopy and optical microscopy were used to characterize the composition and distribution of corrosion products inside growing filaments. The filament head contains water (OH stretching modes, 3000-3600 cm^{-1}), and corrosion products based on aluminium oxide with both tetrahedrally (840 cm^{-1}) and octahedrally (600 cm^{-1}) coordinated Al^{3+}, and with some hydroxyl group content (3075, 1420, 1164 cm^{-1}). Remarkable is the prominent presence of structural motifs as in γ-AlH_3 (1045, 1495 cm^{-1}). The tail contains predominantly aluminium oxide with octahedrally coordinated Al^{3+} and in addition carbonate (1100 cm^{-1}) and aluminium chloride (347 cm^{-1}). Video recordings of the active filigree show hydrogen evolution inside the active head and a very fast precipitation of corrosion products. Re-dissolution, transport and re-formation of the corrosion products is also observed, accompanying start-stop-cycles of the propagation of FFC; this mechanism leads to wavy surface morphologies by lifting of certain coating areas after the passage of the corrosion front as evidenced by 3D optical profilometer analysis. When exposed to the acidic head conditions for a sufficient time, the initiation of other forms of localised corrosion, such as pitting, is possible, which in turn facilitates further propagation of the filament. The in situ detection of hydride which transforms into the typical aluminium corrosion products in due course points to a prominent role of hydride as intermediate in the aqueous corrosion of aluminium.

1 Introduction

Reported already in the 1940s and 1950s,[1,2] filiform corrosion (FFC) of a coated metal has become a concern in the building and automotive industry. This localized corrosion process usually takes place on coated metals. In the most severe cases, FFC can lead to flaking of the coating and sometimes to initiation of other types of corrosion such as pitting or intergranular corrosion.[3] FFC typically initiates from coating defects. In the coating defect the cathodic oxygen reduction reaction (ORR) and hydrogen evolution reaction (HER) take place until a differential aeration cell is build where the combination of low concentration of oxygen far from the defect combined with a high concentration of oxygen close to the defect gives rise to a difference in electrode potential between the two regions that now constitute the corrosion cell leading to the start of the filament propagation.[4] Once the propagation has started, the inside of the filament is characterized by three different environments:[5]

1. An acidic head where the dissolution of the substrate metal takes place (anodic reaction).
2. A neutral to alkaline back of the head where the ORR takes place.
3. A tail filled with corrosion products.

The currently accepted FFC mechanism on aluminum alloys is shown in Fig. 1.[5]

Since the 1980s, many authors have studied FFC and the effect of substrate and pretreatment,[6–8] metallurgical parameters,[9] corrosion products,[10] and other features such as the kinetics,[11,12] effect of intermetallic particles (IMP),[13] effect of surface treatment as machining,[14] and enrichment of alloying elements such as Cu.[15] Furthermore, the in the presence of a near surface deformed layer (NSDL) induced by thermo-mechanical processing, shear deformation and machining, a microstructure that is very different from the bulk alloy is present, which increases the susceptibility to FFC.[14,16–20] The mechanism in this case, however, is slightly different. The NSDL is electrochemically more active

[a] Department of Materials Science and Engineering, NTNU, Norwegian University of Science and Technology, 7491 Trondheim, Norway. E-mail: FFC-Raman@the-passivists.org
[b] SINTEF Industry, 7465 Trondheim, Norway.

† Electronic Supplementary Information (ESI) available: Scheme of the setup. Additional surface morphology data. Detailed discussion of assignment of Raman spectra, including some additional spectra. Video showing in situ activation and deactivation of a filament. See DOI: 00.0000/00000000.

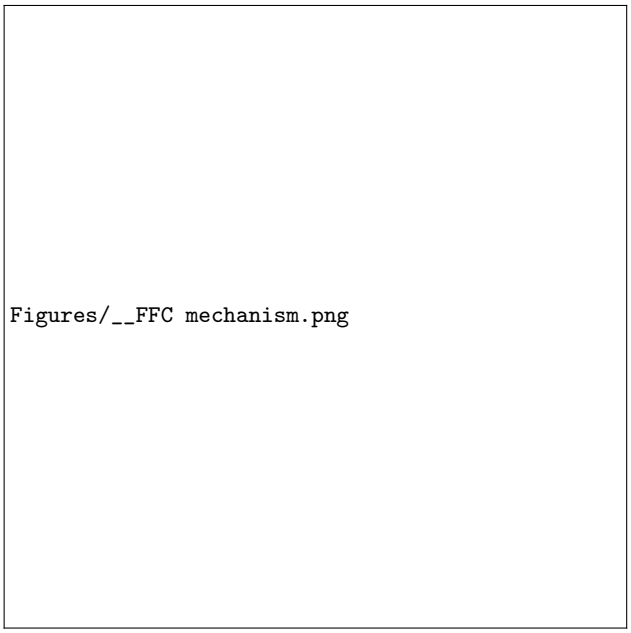

Fig. 1 FFC propagation mechanism on coated aluminium alloys showing the corrosion products filling the tail, the corrosion cell in which the anodic (metal dissolution) and cathodic (oxygen reduction) reactions take place.[5] Reprinted from Shreir's Corrosion, Vol. 2, H.N. McMurray, G. Williams, chapter 2.14 - Under Film/Coating Corrosion, pp. 988-1004, Copyright (2010), (https://doi.org/10.1016/B978-044452787-5.00040-8) with permission from Elsevier, https://www.elsevier.com/.

than the bulk of the material,[21,22] and acts as a sacrificial anode. In this case, the attack is usually limited to the NSDL itself. However, it is not uncommon to observe a successive-pitting type of corrosion.[12,19,23] The mechanism proposed consists of two steps, (i) the consumption of the NSDL by the passage of the corrosion front, and (ii) the passage of a new corrosion front in which the corrosion products generated during the first step are chemically dissolved or mechanically broken and the matrix surface can be subject of pitting corrosion.[24] Furthermore, the successive-pitting mechanism can take place only when the surface is not cathodically protected by the presence of a NSDL. Both IMPs and NSDL near the surface are industrially removed by pretreatment such as alkaline etching.[25]

A recent series of studies of FFC on coated Mg alloys showed a modification of the schematic mechanism as sketched above, and highlighted also the importance of the chloride concentration.[26,27] On magnesium, HER has been noted to drive a cathodic delamination type of process; the dominance of anodically driven FFC over cathodic delamination strongly depended on the salt used for initiation.[28] For cathodic delamination, a recent work highlights the importance of cation insertion into the intact interface,[29] a step which could also play a role in FFC.

While there are a number of studies involving post-mortem analysis,[6–9,14–21] the actual transformation between corrosion products forming in the head region to the final tail region has mainly been studied by Kelvin probe or other electrochemical techniques.[11–13,26–28] Acoustic emission is also becoming an increasingly useful in situ technique.[30] In situ optical microscopy permitted direct observation of the morphology during propagation.[26,27] Two studies have investigated FFC in situ,[31] or quasi in situ,[10] by infrared spectroscopy on aluminium. In situ and operando vibrational spectroscopy gives on the other hand significant advantages for obtaining direct insight into reactions mechanisms and processes,[32,33] such as the study of solvation,[34,35] reaction intermediates in electrocatalysis or corrosion,[36–39] oxides forming in electrocatalytical processes,[40–42] corrosion and oxidation products,[43–48] cathodic delamination,[49] or corrosion inhibitors.[50,51] Raman spectroscopy as a vibrational spectroscopic method in a confocal microscope combines the possibility of optical imaging with information related to chemical composition of corrosion products on the μm length scale; it can be applied in the field,[52] and is a popular tool, e.g. in electrochemistry,[53] or atmospheric corrosion.[54] Raman spectroscopy is also widely applied to study corrosion products of aluminium.[55–58]

Main purpose of this work was to follow FFC in situ, in order to elucidate the chemical reactions in this complex process in more detail. The main goal was to observe in situ the formation of corrosion products particularly in the active head of the filament and possibly to detect unstable intermediate species. To that end, aluminium samples were coated with a weak transparent model coating, and a defect was prepared in the coating by scratching. In the defect, FFC was initiated by exposure to concentrated hydrochloric acid. The evolution of filaments was followed in situ in an optical and confocal Raman microscope after placing the sample in chamber with controlled relative humidity of >80%. After a description of the samples studied (section 2.1) and the methods used (section 2.2), this work proceeds in a slightly unusual way with the description of the results and their discussion in section 3 with a structure inspired by the nature of the FFC process. After a presentation of the results of the morphology (section 3.1), the spectroscopic results are described and spectra on the whole are interpreted (section 3.2). The discussion of the processes in the filament head (section 3.3) and filament tail (section 3.4) is presented together with a brief description of the spectroscopic evidence in the respective part of the filament; the respective sections also contain a comparison with existing literature. Finally, the discussions of the results from head and tail are merged into a mechanistic picture of FFC (section 3.5), before the manuscript concludes (section 4).

2 Materials and Methods

2.1 Materials

A hot rolled AA3005 aluminium alloy provided by Speira was used for this study. The composition is shown in Table 1. The manufacturing of the sheets consisted of hot rolling to 3.5 mm thickness, followed by cold rolling to a final thickness of 0.68 mm and annealing at 224-230°C.

2.2 Methods

Aluminium sheets of 3×3 cm^2 were cleaned with acetone and ethanol using laboratory paper and dried with compressed air. The samples were then coated with Paraloid B 48, a commercial acrylate-based transparent weak model coating purchased from

Table 1 Composition of AA3005 samples as determined by inductively coupled plasma optical emission spectroscopy at the manufacturer.

Elements	wt.%
Si	0.49
Fe	0.58
Cu	0.22
Mn	1.08
Mg	0.35
Cr	0.041
Zn	0.14
Ti	0.017

Kremer Pigmente. The pellets were dissolved in toluene to a polymer concentration of 33 wt.-%. The coating was applied to the sample surface by spin-coating with a program that allowed to deposit a ca. 20 μm thick layer. Raman experiments at the polymer/metal interface require sufficient transparency of the coating, so that the metal surface can be both illuminated and Raman scattered light from the region can be collected.

An artificial defect was prepared in the coating with an Erichsen Model 639 Corrocutter according to the Qualicoat standard procedure for FFC testing.[59] FFC was initiated by dropping a few drops of HCl (37%) on the artificial defect which was allowed to react for 1 min before removing the solution very gently with a laboratory paper. The sample was left in ambient air for 30 min before putting it into a homemade in situ Raman cell at 40°C and 86(±5)% relative humidity. The cell was based on a setup previously used to study cathodic delamination.[49] A schematic representation is shown in ESI-Fig. 1†. A saturated KCl solution was used to fix the relative humidity.[60] The base of the cell was made in a way that water could be fluxed in it in order to keep the temperature at 40°C.

Visual images, videos, and Raman spectra were recorded in this cell in a confocal Raman microscope (WITech alpha 300 microscope) equipped with a 532 nm laser excitation. The spectra were acquired using 10× and 50× objectives. A laser power of 30 mW was used in all the measurements unless differently specified. Typical integration times were 2 s with 10 accumulations per spectrum. In different cases, instead of a single spectrum measurement, an area scan or a depth scan analysis was performed. For this purpose, 50 Raman spectra were collected to construct one line and 50 lines were used to build a 2-dimensional image in which each pixel is represented by a Raman spectrum. Cosmic ray removal, background subtraction, and true component analysis followed by de-mixing were performed in the instrument manufacturer's software to identify the chemical composition and to build a distribution map of different components such as coating, corrosion products, and metal matrix. An area scan represents a 2D image of a horizontal section while a depth scan represents a 2D image of a vertical section of the sample. All the data analysis was done using the WITech Project Plus Version 5.2.16 Software.

The surface morphology of coated samples was studied using a 3D optical profilometer model Contour GT -K manufactured by Bruker. All the 3D profiles were measured post-mortem i.e., all the filaments were inactive.

For some samples, the coating was removed using tweezers, and the corrosion products were collected and analyzed with Raman spectroscopy.

Raw data from this study is available online.[61]

3 Results and discussion

3.1 Filament morphology

Fig. 2b shows the intensity of the Raman signal from the coating obtained from a depth scan of the filament in Fig. 2a along the propagation direction of the filament. This figure shows that the part of the coating lifted most is the head of the filament. Therefore, there must have been a coating relaxation after the passage of the corrosion front, and consequently, the filament tail cannot be completely filled with corrosion products, which is contrary to the textbook representation in Fig. 1.

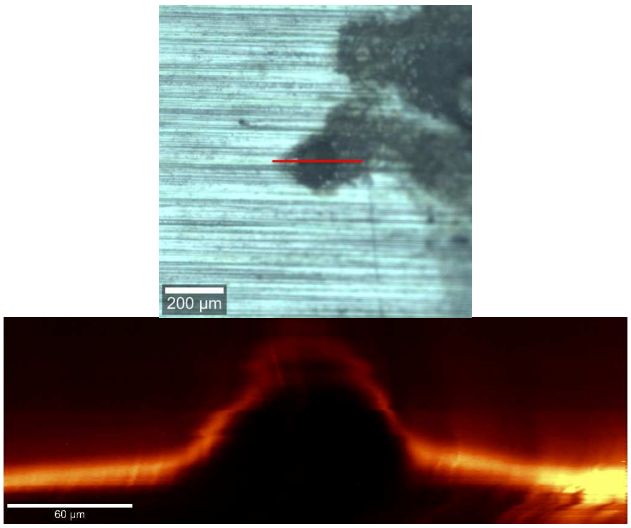

Fig. 2 (Top) Filament growing from artificial scratch (right-hand side, not visible in image) and (Bottom) distribution of coating signal from depth profile in the confocal Raman microscope (high brightness - large coating signal). The position of the depth scan is shown by the red line in (a).

Fig. 3 shows 3D pictures of two different filaments measured with an optical profilometer. These two filaments represent two prototypical cases of different morphologies observed after deactivation. All filaments show either of these two morphologies after deactivation; at least three different occurrences of each type have been observed. The first type (example in Fig. 3a) are filaments of 50-100 μm width, where the high ($\sim$25 μm) coating lifting in the head suggests that the corrosion products have deposited mainly in this region. For filaments with this morphology, it is evident that the tail contains fewer corrosion products than the head since the coating on top is lower than the head. The second type (example in Fig. 3b) shows narrower filaments of a width $<$30 μm, with a height decreasing along the filament from tail to head.

This morphology of the tail was similar for all the analysed filaments, i.e. for filament morphologies of the first and second type. Along the filament, there are mature regions where the lifting of the coating is more pronounced and regions where lifting is

less pronounced. An example of a long filament with alternating regions is shown in ESI-Fig. 2†. Two types of morphology have also been observed after FFC on carbon steel coated with a thin epoxy-based coating,[62] one of those closely resembling the wave-like patterns observed here. Different directions of O_2 ingress have been suggested to cause different morphologies.[62] For cathodic delamination, a strong dependence of delamination rate on morphology was found,[63] which shows that disbonding kinetics itself is affected by the morphological features of the surface.

Two other important features not present in Fig. 1 are bubble formation in different regions of the filament including the head, and the precipitation of corrosion products in the local anode region. From the video of the propagating filament which is part of the ESI† (description in ESI-section 4), it is clear that the precipitation of corrosion products can take place close to the propagation front in proximity to what closely resembles an active pit. Probably the concentration of the different salts in the region near the pit becomes so high that precipitation of corrosion products takes place immediately after the product of solubility is reached and a nucleation site is present. The implications of gas evolution will be discussed in detail in section 3.3.

3.2 Assignment of spectral features

Table 2 Raman peak positions of the aluminium/coating interface containing corrosion products, as observed in this work, together with the tentative empirical assignment. ν - stretching mode, δ - deformation mode. Index s - symmetric, index as - antisymmetric

Peak cm^{-1}	Species	Mode	Ref.
347	Al−Cl	A_g	64–66
521	$[Al(OH_2)_6]^{3+}$	A_g	67,68
600	AlO_6 octahed.	ν(Al−O), E_g	69,70
840	AlO_4 tetrahed.	ν(Al−O)	71
1045	γ-AlH_3	A_{1g}(Al−H_3/H_4)	72–74
1100	CO_3^{2-}	ν_s	75,76
1164	Al-O surface	Surface phonon + δ((Al)−OH)	77,78
1420	(Al)-OH	δ(OH)	
1495	γ-AlH_3	B_{1g}(Al−H_3)	72–74
1607	bound H_2O	δ(OH_2)	71,79
3075	(Al)-OH	ν(OH)	35
3000-3600	H_2O, OH	ν(OH)	34,35

Spectra recorded in the different stages of FFC are shown in Fig. 5 and 6. As exemplified by the area scan in Fig. 5, the Raman spectra collected throughout this study can be divided into three groups, (i) those characteristics for the intact model coating, (ii) those characteristics for the corroding metal/polymer interface and (iii) featureless spectra of the metal. The spectrum of the non-degraded coating is known from reference measurements (ESI-section 3)†, and the spectrum of the metal does not show peaks; most relevant for the understanding of the corrosion processes is the component of the interface. The latter is represented by the blue area in Fig. 5d which is a map of the horizontal section of the filament head shown in Fig. 5b; this spectrum will be prototypically used for the discussion of the assignment.

Before proceeding to a discussion of the chemical processes in the different stages of FFC, it is crucial to assign the spectral features to chemical species. Table 2 lists all the spectral features observed in the system here, together with a tentative empirical assignment. The full reasoning behind the assignment is given in ESI-Section 3†. Obvious is the prominent presence of OH stretching modes (3000-3600 cm^{-1}) in the head with a shape typical for water, and a discrete peak at 3075 cm^{-1} assigned to an OH group or ion.[34,35] We further notice distinct differences to the literature spectra of different aluminium (oxy)hydroxides, such as gibbsite γ−$Al(OH)_3$, bayerite α-$Al(OH)_3$, boehmite γ−AlOOH and diaspore α−AlOOH.[80–82] On the other hand, there is the presence of typical modes from aluminium oxides indicating Al^{3+} in octahedral (≈600 cm^{-1}) and tetrahedral (≈840 cm^{-1}) coordination.[80,83–88] Peaks at 1420 cm^{-1} and 1164 cm^{-1} have strong contributions of Al-O-H deformation.[77,83] There is a very close similarity in shape, intensity, and position between peaks observed in γ−AlH_3 and the peaks at 1045 and 1495 cm^{-1} in the head, which is why these peaks are assigned to hydride species.[72,73] The very broad peak at 1100 cm^{-1} in the tail is in a region typical for carbonate stretching modes embedded in aluminium oxyhydroxides.[75,76,89] Finally, the lowest distinct peak in the tail at 347 cm^{-1} is assigned to Al-Cl-related modes.[65,90,91]

Based on the spectral assignments, the corrosion products in the head are based on aluminium oxides, containing structural motifs as in γ-AlH_3, and different types of hydroxyl groups. The oxide structures contain both tetrahedrally and octahedrally coordinated aluminium. As there are large differences to the spectra of typical aluminium (oxy)hydroxides, these compounds cannot be typical for the structures observed here. The spectra in the tail point to carbonate and chloride containing aluminium oxide, with predominantly octahedrally coordinated aluminium.

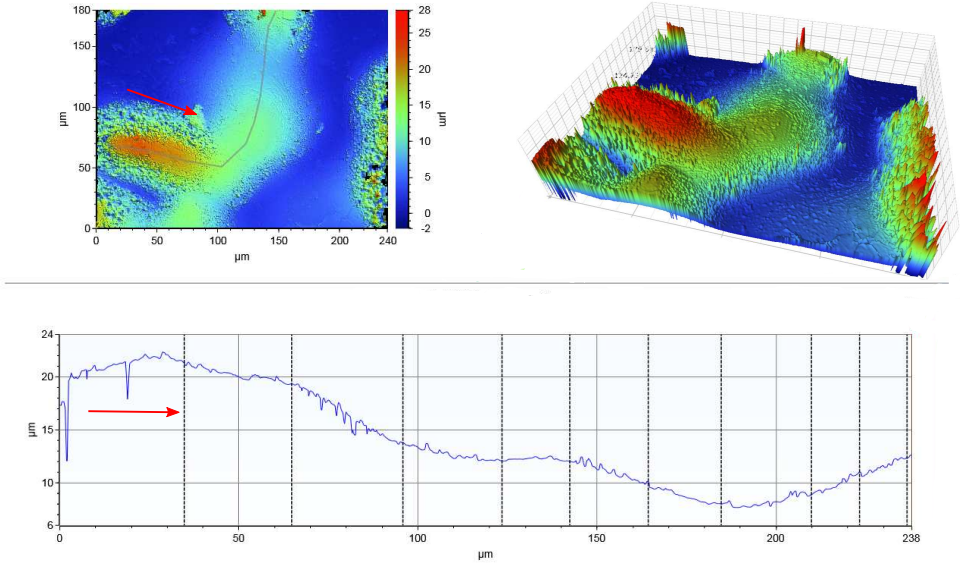

(a)

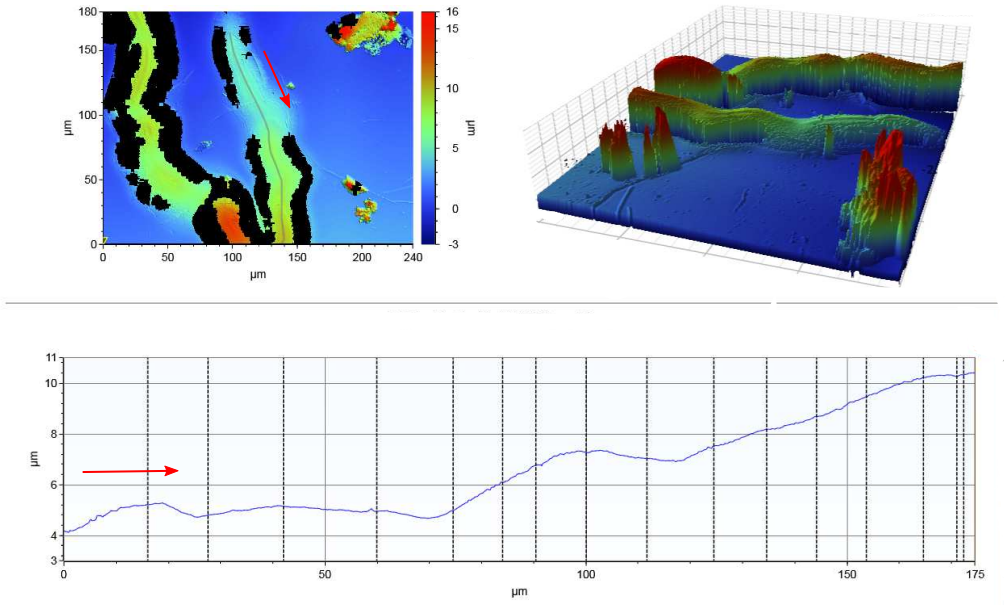

(b)

Fig. 3 Morphology of two different inactive filaments [(a) and (b)] measured with a 3D optical profilometer after exposure to high humidity conditions, with coating on top. The graph at the bottom of the respective panel shows the height profile indicated by the grey line (representing the filament propagation direction) in the respective image. The image on the left represents a surface view, and the image on the right the same area in a 3D view. The color coding in the height profile is the same for the left and the right image in the respective panel. The red arrow represents the head-to-tail direction. On black pixels, no height information was obtained.

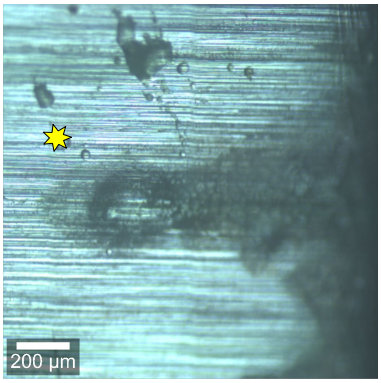

(a)

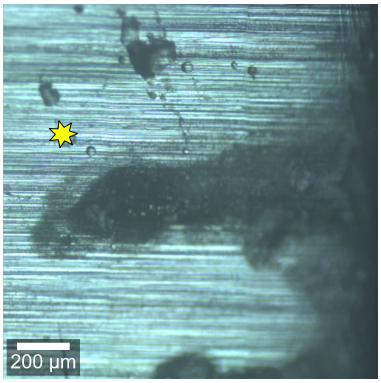

(b)

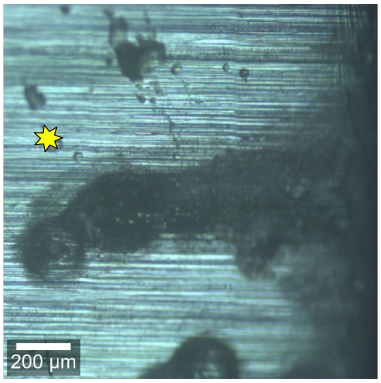

(c)

Fig. 4 Filament propagation. The same area imaged every 24 h. The yellow star can be used as a reference point to facilitate the following of the filament growth.

3.3 Head of the filament

Fig. 5a shows a filament propagating from an artificial scratch. Fig. 5b shows a higher magnification of the head of the main filament shown in Fig. 5a (indicated by the red arrow) and the position of the area scan (square). Fig. 5c shows the spectra of two of the three main components and the bitmap with the position of the respective component; the metal matrix shows essentially a flat, noisy spectrum which is not displayed here. The positions of the main observed Raman peaks are summarized in Table 2.

As obvious from the assignment in section 3.2 and the compilation in Table 2, the spectra from the head show evidence for the presence of aluminium oxides with some hydroxide, and aluminium hydride. While the former are very well documented in the literature in a variety of different situations, the latter is not. However, the continuous formation of aluminium hydride particles during aluminium dissolution under alkaline conditions was evidenced by secondary ion mass spectrometry (SIMS).[92,93] More generally, the presence of hydride was reasoned to be important to explain the corrosion potential of aluminium.[94]

Mechanistically, the formation of adsorbed hydrogen atoms, $H^+ + e^- \longrightarrow H_{(ads)}$, must be the first step of the HER, and as discussed in section 3.1, there is evidence for bubble formation in the region of the head. Hydride can thus form as a side reaction of the HER by the reaction of aluminium with adsorbed hydrogen,[92,93]

$$Al_{(s)} + 3H \longrightarrow AlH_{3(s)}. \quad (1)$$

Alternatively, the hydride formation may be seen as an electrochemical reduction of H^+,

$$Al^{3+}_{aq} + 3H^+_{aq} + 6e^- \longrightarrow AlH_{3(s)}. \quad (2)$$

The fact that hydride formation is observed in the head region which is supposed to be anodic points more to a chemical mechanism [reaction (1)] of formation rather than to an electrochemical mechanism [reaction (2)]. The forming hydride-containing species must be more than a surface hydride, judging by the depth resolution of a confocal Raman microscope, and also by the thickness of the hydride-containing region in the spectra, e.g. the depth scan in ESI-Fig. 5†. Rather, this must be a solid phase extending over at least many tens of nanometres.

This hydride-containing solid oxidises stepwise in a reaction with water to the aluminium [(oxy)hydr]oxides, with steps of the type

$$AlH_{3(s)} + H_2O_{(l)} \longrightarrow H_2Al{-}OH_{(s)} + H_{2(g)}, \quad (3)$$

again yielding H_2 as a product. It is thus not a priori clear whether the observed hydrogen bubbles originate from the electrochemical HER, or a chemical step such as reaction (3). Most likely, both will contribute. In this context, it must be stressed that at typical corrosion potentials of aluminium, electrochemical hydrogen evolution is thermodynamically possible. It is therefore not a contradiction to observe hydrogen also around the anode. Aluminium does furthermore show the negative difference effect, i.e. increased rates of hydrogen evolution with increasing electrode potential.[95]

Transport of water into the filament is needed for the hydride hydrolysis [reaction (3)]. Because water is present only in small amounts, hydrides can build up to large amounts as observed. Water transport kinetics may also contribute to the overall kinetics. The lack of water has also been used to reason for the presence of start-stop cycles in cathodic delamination.[49]

Aluminium hydrides may play a more general role as intermediates in aluminium corrosion than previously thought. Here, the hydrides are formed in the head, which must be acidic, because of anodic aluminium dissolution and the accompanying aluminium hydrolysis equilibrium. In contrast to the in situ observation under acidic conditions in this work, previous analysis by electrochemical methods indicated no presence of hydrides under conditions of alkaline etching below a pH of ≈11.5.[92,93] Furthermore, the open circuit potential analysis conducted in the 1970s give no reason to believe that hydride presence should be restricted to a certain pH;[94] we, therefore, expect a more general presence of hydrides when aluminium is exposed to aqueous solutions. Aluminium hydrides are, however, difficult to observe because of their reactivity. Indeed, an impedance study suggested multistep dissolution of Al in hydrochloric acid, for which an Al^+ intermediate had been postulated.[96] However, a hydride intermediate may also explain the multistep nature of the observed dissolution.

The effect of H_2 bubbles on filament propagation is worth discussing. The presence of pits and hydrogen evolution has been reported a few times in literature[97,98] but has traditionally been considered as negligible. More recent works on related systems, however, point to a more prominent involvement of hydrogen evolution under certain conditions.[28,99] The presence of a pit at the tip of the filament head (i.e., of what is considered to be the anodic region of the "macro" corrosion cell) can affect the whole system in different ways:

1. The H_2 bubbles formed inside the pit will cause a convective motion that will stir the solution leading to a more uniform pH and composition of the corrosion cell. In a more neutral environment, the precipitation of aluminium-based corrosion products is favoured. The effect of induced convection also contributes outside the pits.

2. The presence of an electric field in close proximity to the pit will cause the migration of positively charged ions toward the surface just outside the pit (or toward the pit's walls). Since the pit is at the tip of the head, this motion will be in the opposite direction with respect to the migration caused by the presence of the electric field in the macroscopic corrosion cell. Thus creating milder conditions would also facilitate the precipitation of corrosion products.

3. The high concentration of ions in the proximity of the pit facilitates the precipitation of corrosion products.

Furthermore, the H_2 bubbles, regardless of their mechanism of origin, can merge to bubbles with larger volume, accumulate under the coating, and assist in the process of coating detachment. Bubble-assisted coating detachment could explain the voids observed sometimes during the filament propagation (Fig. 4). In this case, the porous layer of corrosion products deposited around

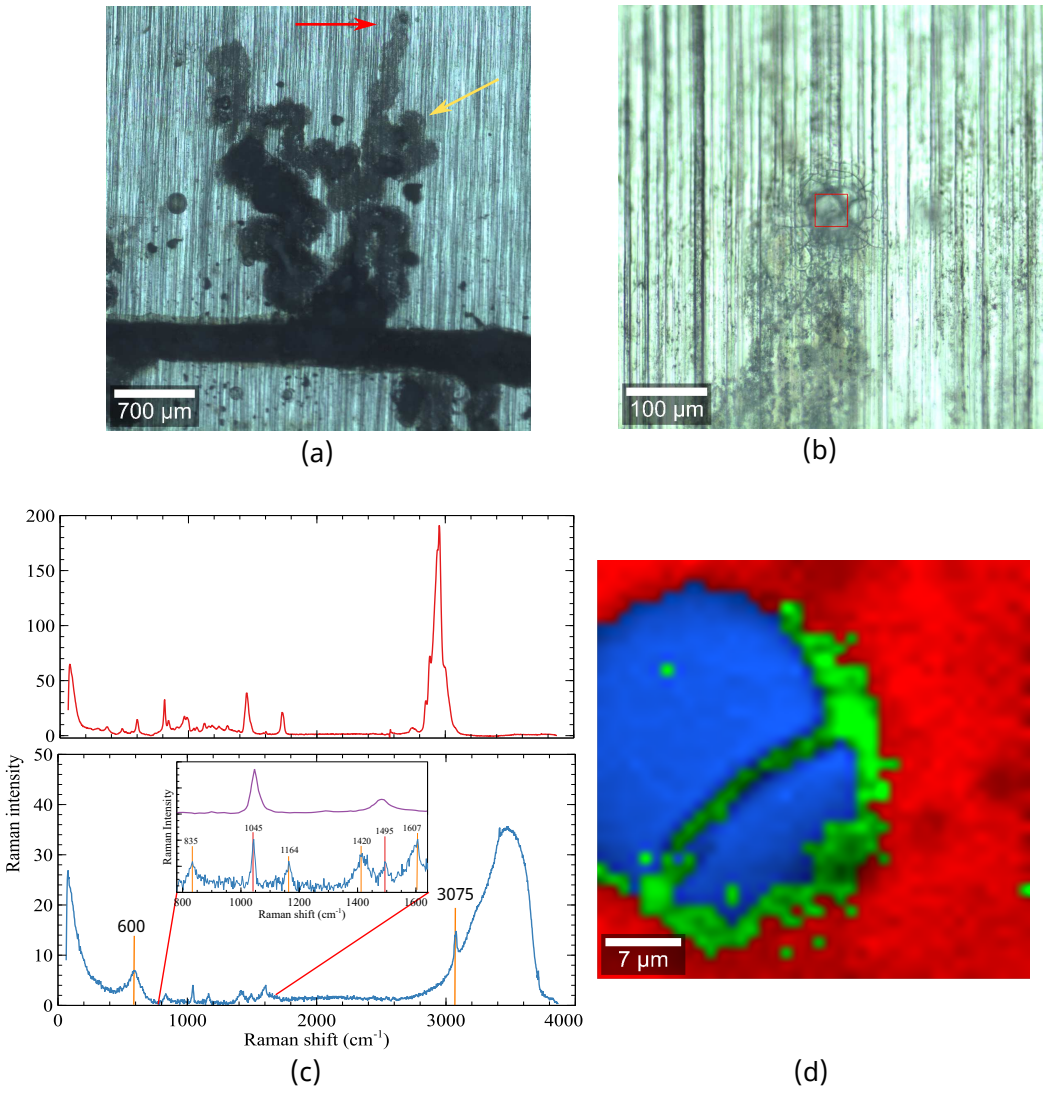

Fig. 5 (a) Low magnification micrograph of filament growing from an artificial defect. (b) Higher magnification of the filament head shown in (a) as indicated by the red arrow. (c) Raman spectra of model coating (red) and corrosion products (blue); the spectrum in purple shown in the inset represents the γ-AlH_3 spectrum from ref.[73]. (d) Combined bitmap file showing the position of coating (red), corrosion products (blue) and metal (green). Peak positions from spectra are compiled in Table 2.

the bubble could act as a capillary canal that induces and facilitates water propagation towards the filament head. When H_2 escapes, either through the coating or the tail of the filament, the precipitation of corrosion products takes place also in the central region of the head. The repetition of this process during the filament propagation could explain the filament tail morphology discussed above with alternating lifted and lower areas.

The presence of IMPs is necessary for FFC to occur.[100] The absence of noble intermetallic particles on Al-Mn alloys led to immunity to FFC.[100] The filaments have a tendency to propagate "jumping" from one intermetallic particle to another.[13] This detrimental effect on FFC resistance caused by the presence of IMP could be on one hand because of the increased potential difference between cathode and anode when noble IMP are involved or on the other hand to the higher amount of H_2 evolution favoured by noble IMP assisting the corrosion process.[101] Most likely is a combination of the two.

A prominent role of hydrogen evolution in the degradation of the metal-coating interface has been suggested in a recent study on the corrosion of aluminium under an epoxy coating.[99] A correlation was observed between the position of blisters and Mg-based IMPs suggesting that HER does not occur only in the proximity of IMPs nobler than the base alloy but also close to less noble IMPs.[99] In this last case the HER would be accompanied by Mg dissolution,[102] or facilitated by the presence of $Mg(OH)_2$.[99]

3.4 Tail of the filament

Fig. 6 shows a magnified image of part of the filament tail presented Fig. 5a (indicated by the yellow arrow) and the respective spectra. The main difference between the two spectra acquired in different regions (one brighter and one darker) is the presence of a peak at ≈350 cm^{-1}. The peak at ≈350 cm^{-1} has been observed also in other dark areas of the filament tail suggesting the accumulation of chloride-based compounds in these

regions. Occasionally, in the same location, peaks at ≈350 cm^{-1} and ≈520 cm^{-1} are observed, the latter indicating the presence of $[Al(OH_2)_6]^{3+}$ (ESI-Fig. 7†). This colocation could either indicate the presence of hydroxychlorides[67,68], or of a local mixture of dissolved aluminium and a chloride-containing species.

In the tail of the filament, the presence of hydroxycarbonates is expected. Aluminium hydroxycarbonates can form at a pH of 6 - 7 and are typically amorphous.[103] The width of the carbonate peak as observed here has been interpreted to indicate an interaction of the carbonate oxygen atoms with the Al^{3+} ion. In this work, this band is more intense when the corrosion products are analyzed separately than in the in situ measurements; possibly the carbonate content increases post-mortem due to the exposure of the corrosion products to atmospheric CO_2. In ZnAl metallic coatings ("galvalume"), the formation of zinc and aluminium hydroxycarbonate was hypothesized; while the formation of zinc carbonates is well-known in zinc corrosion,[104] the formation of aluminium-rich carbonates was not excluded,[105] or qualitatively confirmed without quantitative analysis.[106] On an aluminium alloy in a post-mortem analysis, the presence of aluminium hydroxycarbonate in the tail of filament was also found previously.[10]

Fig. 7 shows the same filament as in Fig. 6 before and after the propagation of a new filigree, initiated from the previous one. In the tip of the head, it has been argued that aluminium-based cations $Al(OH)^{2+}$, $Al(OH)_2{}^{+}$ and polymeric species such as $Al_{13}O_4(OH)_{24}(H_2O)_{12}{}^{7+}$ are formed and migrate toward the back of the head precipitating as an aluminium hydroxide gel into which carbonate and chlorides are incorporated[10]. (A migration may also not be necessary since the tip of the head is moving forward over time). Finally, some chloride ions are released and migrate toward the tip of the head.[10] Nevertheless, the presence of chlorides is observed also after the passage of the corrosion front (Fig. 6) meaning that some part of the chloride-based compounds remains trapped in the aluminium hydroxide gel. The presence of chlorides in the tail was confirmed by proton-induced x-ray emission.[107] It is worth noting that the "new" filament shown in Fig. 7 starts propagating from the region where the presence of chlorides was detected (Fig. 6) as if the presence of chloride-based corrosion products acts as a reservoir of aggressive species able to trigger the initiation of a new filament without the necessity of a transfer to the corrosion front. Because some of the chlorides remain trapped in the corrosion products deposited in the tail, there will always be fewer chloride ions at the corrosion front during the propagation. The decrease in available chloride concentration would lead to filament deactivation.

Deactivation because of chloride consumption is in agreement with observations during accelerated FFC tests. During these tests, the propagation rate decreases with time probably because of a decreasing amount of chloride ions able to reach the tip of the head. A similar mechanism also acts on Mg alloys.[26]

A semiquantitative determination of a composition gradient between head and tail along the filament is prohibitive due to large amount of measurement time needed during which the system would again transform. An additional complication arises from the non homogeneity of the corrosion product distribution inside the filament. The inner part of the filaments is characterized by regions alternating a strong signal form corrosion products with an almost absent signal. Because the propagation mechanism is also function of stochastic events (such as pitting initiation) the amount and distribution of regions with high and low amounts of corrosion products along the filament would differ from filament to filament.

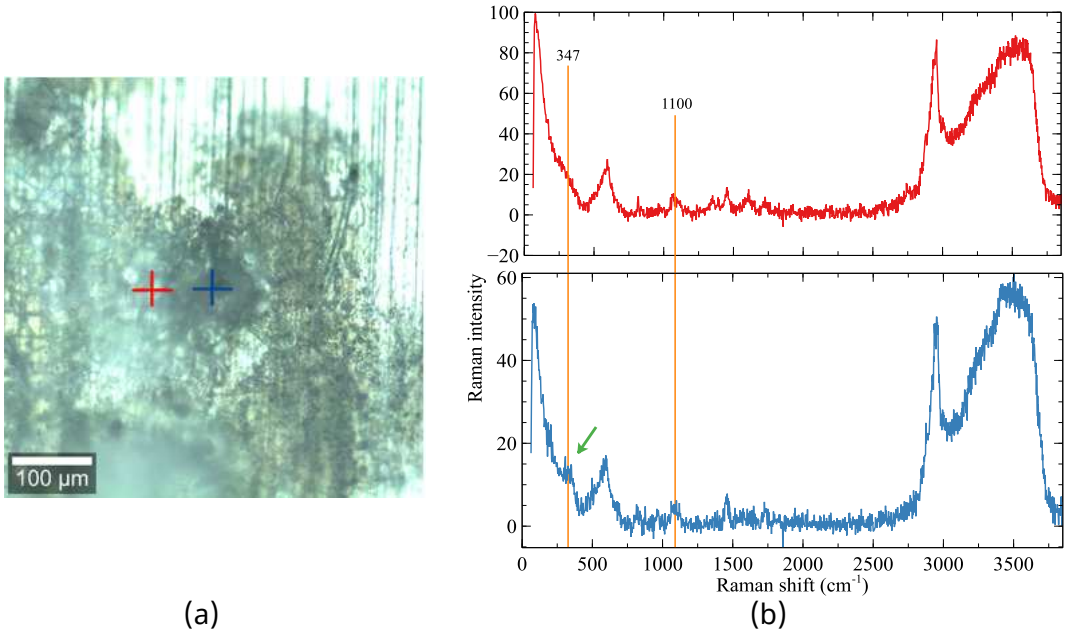

Fig. 6 (a) Part of the tail of the filament shown in Fig. 5(a); (b) Raman spectra at the positions marked by crosses in (a). The green arrow indicates the position of the peak characteristic of the Al−Cl stretching mode. The band shown at 1100 cm^{-1} is representative of the carbonate stretching mode.

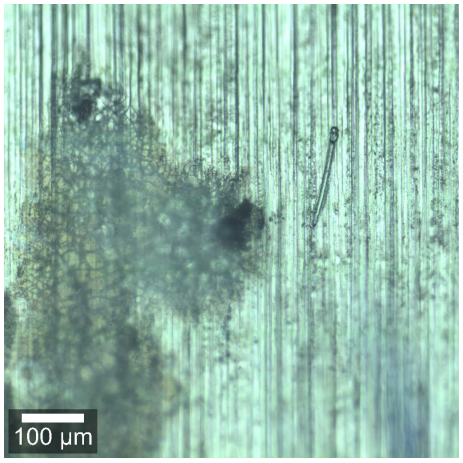

(a)

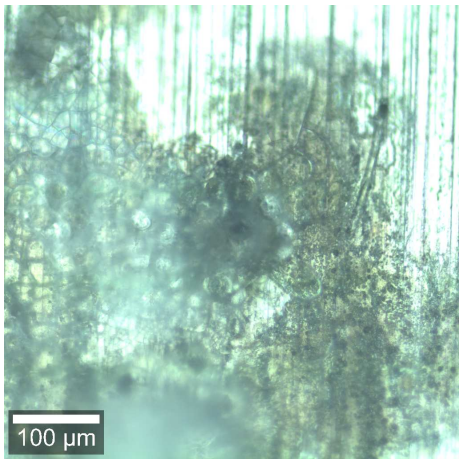

(b)

Fig. 7 Same filament (a) before and (b) after the initiation of a new filigree.

3.5 Revised picture of FFC mechanism

Based on the discussion of the chemical process in head and tail, a refined mechanistic picture of successive-pitting type FFC is shown in Fig. 8. This figure presents a propagating filament at different stages. In addition to the known anodic reactions of aluminium dissolution (labelled "AlD"") and ORR, hydrogen evolution, aluminium hydride formation and hydride decomposition are represented. Aluminium dissolution and the presence of pits in the tip of the head can cause a drastic increase in aluminium ions concentration leading to the precipitation of corrosion products also in the tip and not only in the back of the head where the ORR takes place. The presence of the forming porous corrosion products could favour water transport toward the undamaged part of the coating by capillarity (upper part of Fig. 8; section 3.3). When the coating adhesion in the region highlighted by the blue circle in Fig. 8 is high, the exposure time of the aluminium surface to the electrolyte is high enough to allow the formation of a new macro corrosion cell where the pressure generated by the formation of bubbles and new corrosion products assists the coating inflation and detachment. Hydrogen bubbles can be generated inside the pits or when the aluminium hydride in contact with the aqueous solution is converted into gaseous hydrogen and aluminium hydroxides. When the new macro corrosion cell is formed, the region that was previously the active head transforms into a part of the tail. However, a certain level of active corrosion must still occur since the presence of bubbles and a movement of corrosion products are sometimes observed.

Carbonate is included in the corrosion products here, because atmospheric CO_2 also diffuses into the active region, causing precipitation of carbonate-containing corrosion products above a pH ≈6-7. The exact role of carbonate on the kinetics and morphology in this system is so far unclear; for zinc-based alloys, the role of carbonates is very prominent,[104] though their development is only limited on short time scales.[48,108] Possibly, carbonate formation also plays a role in the propagation and thus ultimately inhibition of FFC. The presence of the hydrides may also facilitate a reaction with CO_2 and solid corrosion products. This point requires dedicated detailed studies.

Pits would initiate after a certain exposure time to the conditions of the anolyte, and not directly at the tip of the head. Pitting initiation would usually require a certain initiation time τ_{crit}, i.e. a certain residence time τ of the material in a critical (acidic) solution. If FFC progress was uniform with velocity v, the length l along the filament direction of the region exposed to the acidified solution would determine the time material is exposed to a given area conditions, $\tau = \frac{l}{v}$. The fact that v varies over time makes this process semi-continuous: material is exposed to the acidic head for a certain time, pitting initiation occurs if $\tau > \tau_{crit}$, and a consequence is the progress of the disbonding front.

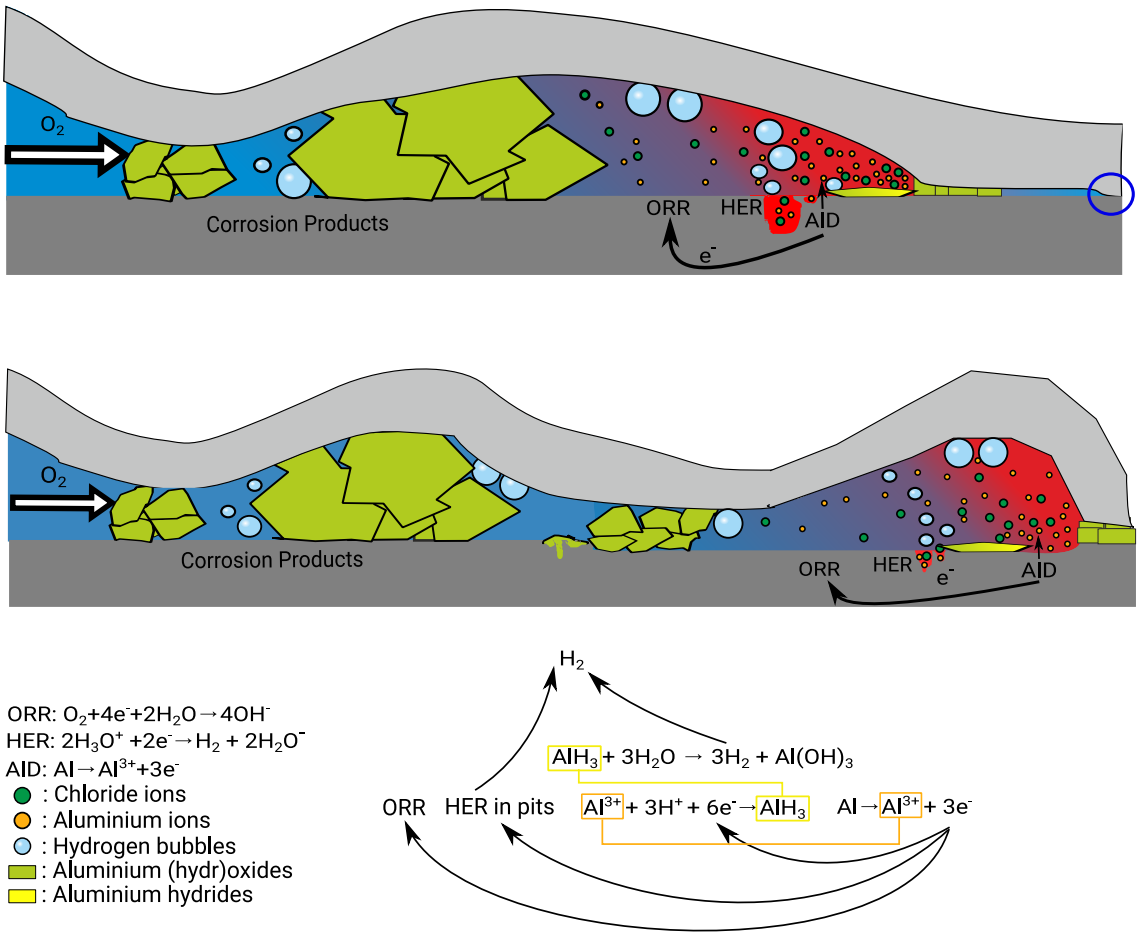

Fig. 8 Proposed mechanism of filament propagation at different times, where the top image precedes the bottom image.

4 Conclusions

1. In situ and operando Raman spectroscopy during FFC under a weak model coating shows evidence for the formation of aluminium hydride in the acidic head region of FFC. As no evidence is found for the presence of hydrides in the corrosion products in the tail, these hydrides must transform into hydroxides which later condense into oxides in the FFC propagation process. On the other hand, carbonates are included in the corrosion products in the tail. Overall, the presence of hydrides as intermediates may be more prominent in the aqueous corrosion of aluminium than previously envisaged.

2. Hydrogen evolution must have an important role in the propagation mechanism, both for the transport of species, the coating detachment, corrosion product formation and precipitation. Possible chemical decomposition of the formed hydrides under the evolution of hydrogen may explain the observation of hydrogen evolution in regions close to the anode.

3. The re-dissolution and lateral displacement of corrosion products inside an active filament are possible. Video observations show that during the filament propagation, (i) the precipitation, re-dissolution and displacement of corrosion products take place inside the filament tail, and (ii) the precipitation of corrosion products is possible also in the filament head before it sets in the filament tail. The species transported by diffusion or convection from the tail toward the head can act as nucleation sites for the precipitation of corrosion products.

4. The presence of two different filament head morphologies after the filament deactivation suggests the possibility of different deactivation mechanisms.

5. Initiation of pitting corrosion, and possibly other forms of localised corrosion, is possible if a surface area is exposed for a sufficiently long time to sufficiently aggressive conditions. Limited availability of certain species (e.g., H_2O) in this system may lead to pit deactivation, triggering the successive pit initiation, propagation and deactivation which is observed here and in other systems.

Author Contributions

Conceptualisation (AE), data curation (EM), formal analysis (EM, AE), funding acquisition (OL, AE), investigation (EM), methodology (AE), supervision (AE, OL), visualisation (EM, AE), writing of the original draft (EM), reviewing and editing (AE, EM, OL).

Conflicts of interest

There are no conflicts to declare.

Acknowledgements

This work was part of the project “Coated Recycled Aluminium - developing surfaces for well-adhering and corrosion resistant coating systems” supported by the Research Council of Norway (No. 309875), Hydro and Speira. The authors acknowledge Johannes Ofstad for helping with the Raman measurements, and Øystein Gjervan Hagemo for assisting with the designing of the cell for the in situ Raman analysis.

Notes and references

1 C. Sharman, *Nature*, 1944, **153**, 621–622.
2 M. Van Loo, D. D. Laiderman and R. R. Bruhn, *Corrosion*, 1953, **9**, 277–283.
3 J.-O. Nilsson, Proceedings of Eurocorr 2019, Madrid, Spain, 2019, p. 222366.
4 R. T. Ruggeri and T. R. Beck, *Corrosion*, 1983, **39**, 452–465.
5 H. N. McMurray and G. Williams, in *Shreir’s Corrosion*, ed. B. Cottis, M. Graham, R. Lindsay, S. Lyon, T. Richardson, D. Scantlebury and H. Stott, Elsevier, Oxford, 2010, ch. 2.14 - Under Film/Coating Corrosion, pp. 988–1004.
6 H. Leth-Olsen, *PhD thesis*, NTNU, Norwegian University of Science and Technology, Trondheim, Norway, 1996.
7 C. Glover, M. Lim, G. Post, M. Mayo and J. Scully, *Corrosion*, 2019, **75**, 1513–1526.
8 O. Lunder, K. F. Heen and K. Nisancioglu, *Corrosion*, 2004, **60**, 622–631.
9 A. Afseth, J. Nordlien, G. Scamans and K. Nisancioglu, *Corros. Sci.*, 2002, **44**, 2491–2506.
10 N. Le Bozec, D. Persson, A. Nazarov and D. Thierry, *J. Electrochem. Soc.*, 2002, **149**, B403.
11 G. Williams and H. N. McMurray, *J. Electrochem. Soc.*, 2003, **150**, B380.
12 H. McMurray, A. Holder, G. Williams, G. Scamans and A. Coleman, *Electrochim. Acta*, 2010, **55**, 7843–7852.
13 C. Senöz, S. Borodin, M. Stratmann and M. Rohwerder, *Corros. Sci.*, 2012, **58**, 307–314.
14 B. Liu, X. rong Zhou and X. xin Zhang, *Trans. Nonferrous Met. Soc. China*, 2020, **30**, 2056–2066.
15 M. Halseid, J. T. B. Gundersen, Ø. Bauger and T. Hentschel, *Surf. Interface Anal.*, 2019, **51**, 1225–1230.
16 H. Leth-Olsen and K. Nisancioglu, *Corros. Sci.*, 1998, **40**, 1179–1194.
17 H. Leth-Olsen, A. Afseth and K. Nisancioglu, *Corros. Sci.*, 1998, **40**, 1195–1214.
18 H. Leth-Olsen, J. H. Nordlien and K. Nisancioglu, *Corros. Sci.*, 1998, **40**, 2051–2063.
19 A. Afseth, J. Nordlien, G. Scamans and K. Nisancioglu, *Corros. Sci.*, 2001, **43**, 2093–2109.
20 A. Afseth, J. Nordlien, G. Scamans and K. Nisancioglu, *Corros. Sci.*, 2001, **43**, 2359–2377.
21 F. Andreatta, A. Lanzutti, S. Maschio and L. Fedrizzi, *Surf. Interface Anal.*, 2019, **51**, 1240–1250.
22 B. Liu, X. Zhang, X. Zhou, T. Hashimoto and J. Wang, *Corros. Sci.*, 2017, **126**, 265–271.
23 Y. Liu, T. Hashimoto, X. Zhou, G. E. Thompson, G. M. Scamans, W. M. Rainforth and J. A. Hunter, *Surf. Interface Anal.*, 2013, **45**, 1553–1557.
24 H. N. McMurray, A. J. Coleman, G. Williams, A. Afseth and

G. M. Scamans, *J. Electrochem. Soc.*, 2007, **154**, C339.
25 E. Mysliu, K. S. Storli, E. Kjørsvik, O. Lunder and A. Erbe, *J. Electrochem. Soc.*, 2023, **170**, 011503.
26 C. Kousis, P. Keil, N. M. Hamilton and G. Williams, *Corros. Sci.*, 2022, **206**, 110477.
27 C. Kousis, N. McMurray, P. Keil and G. Williams, *Corrosion*, 2020, **77**, 156–167.
28 G. Williams, C. Kousis, N. McMurray and P. Keil, *npj Mater. Degrad.*, 2019, **3**, 41.
29 N. Khayatan and M. Rohwerder, *Corros. Sci.*, 2022, **202**, 110311.
30 C. Abarkane, A. Florez-Tapia, J. Odriozola, A. Artetxe, M. Lekka, E. García-Lecina, H.-J. Grande and J. Vega, *Corros. Sci.*, 2023, **214**, 110964.
31 N. Le Bozec, D. Persson and D. Thierry, *J. Electrochem. Soc.*, 2004, **151**, B440.
32 G. Grundmeier and M. Stratmann, *Annu. Rev. Mater. Res.*, 2005, **35**, 571–615.
33 A. Erbe, S. Nayak, Y.-H. Chen, F. Niu, M. Pander, S. Tecklenburg and C. Toparli, in *Encyclopedia of Interfacial Chemistry*, ed. K. Wandelt, Elsevier, Oxford, 2018, ch. How to Probe Structure, Kinetics, and Dynamics at Complex Interfaces In Situ and Operando by Optical Spectroscopy, pp. 199 – 219.
34 A. Erbe and S. Nayak, in *Encyclopedia of Solid-Liquid Interfaces*, ed. G. Bussetti, K. Wandelt, M.-P. Gaigeot, G. Andersson, H. Bluhm, M. Mezger and D. Starr, Elsevier, Oxford, UK, 2023, ch. Understanding water on surfaces, electrodes, and in bulk by vibrational spectroscopies, pp. in press, DOI: 10.1016/B978–0–323–85669–0.00035–0.
35 B. A. Gaweł, A. Ulvensøen, K. Łukaszuk, B. Arstad, A. M. F. Muggerud and A. Erbe, *RSC Adv.*, 2020, **10**, 29018–29030.
36 T. Begildayeva, J. Theerthagiri, S. J. Lee, Y. Yu and M. Y. Choi, *Small*, 2022, **18**, 2270255.
37 S. Shankar Naik, J. Theerthagiri, F. S. Nogueira, S. J. Lee, A. Min, G.-A. Kim, G. Maia, L. M. Pinto and M. Y. Choi, *ACS Catal.*, 2023, **13**, 1477–1491.
38 S. Nayak, P. U. Biedermann, M. Stratmann and A. Erbe, *Electrochim. Acta*, 2013, **106**, 472–482.
39 S. Nayak, P. U. Biedermann, M. Stratmann and A. Erbe, *Phys. Chem. Chem. Phys.*, 2013, **15**, 5771–5781.
40 M. Rabe, C. Toparli, Y.-H. Chen, O. Kasian, K. J. J. Mayrhofer and A. Erbe, *Phys. Chem. Chem. Phys.*, 2019, **21**, 10457–10469.
41 C. Toparli, A. Sarfraz, A. D. Wieck, M. Rohwerder and A. Erbe, *Electrochim. Acta*, 2017, **236**, 104–115.
42 Y. Deng, A. D. Handoko, Y. Du, S. Xi and B. S. Yeo, *ACS Catal.*, 2016, **6**, 2473–2481.
43 J. Weissenrieder and C. Leygraf, *J. Electrochem. Soc.*, 2004, **151**, B165–B171.
44 C. M. Johnson and C. Leygraf, *J. Electrochem. Soc.*, 2006, **153**, B542–B546.
45 C. Toparli, A. Sarfraz and A. Erbe, *Phys. Chem. Chem. Phys.*, 2015, **17**, 31670–31679.
46 C. Toparli, S. W. Hieke, A. Altin, O. Kasian, C. Scheu and A. Erbe, *J. Electrochem. Soc.*, 2017, **164**, H734–H742.
47 G. Genchev and A. Erbe, *J. Electrochem. Soc.*, 2016, **163**, C333–C338.
48 Y. Chen, P. Schneider, B.-J. Liu, S. Borodin, B. Ren and A. Erbe, *Phys. Chem. Chem. Phys.*, 2013, **15**, 9812–9822.
49 D. Iqbal, A. Sarfraz, M. Stratmann and A. Erbe, *Chem. Commun.*, 2015, **51**, 16041–16044.
50 X. Guo, J. Wang, L. Huang, Y. Wang, L. Ma, D. Zhang and L. Ma, *Front. Mater.*, 2022, **9**, 874899.
51 Y.-H. Chen and A. Erbe, *Corros. Sci.*, 2018, **145**, 232–238.
52 J. Jehlička and A. Culka, *Analyt. Chim. Acta*, 2022, **1209**, 339027.
53 Z.-Q. Tian and B. Ren, *Annu. Rev. Phys. Chem.*, 2004, **55**, 197–229.
54 S. Hosseinpour and M. Johnson, *Materials*, 2017, **10**, 413.
55 S. Mahmood, C. Gallagher and D. Engelberg, *Corrosion*, 2022, **78**, 650–660.
56 E. Michailidou, P. Visser, J. Mol, A. Kosari, H. Terryn, K. Baert and Y. Gonzalez-Garcia, *Corros. Sci.*, 2023, **210**, 110851.
57 T. Takano, H. Matsuya, D. Kowalski, S. Kitano, Y. Aoki and H. Habazaki, *Appl. Surf. Sci.*, 2022, **592**, 153321.
58 S. L. Quaireau, K. Colas, B. Kapusta, B. Verhaeghe, M. Loyer-Prost, G. Gutierrez, D. Gosset and S. Delpech, *J. Nucl. Mater.*, 2021, **553**, 153051.
59 Qualicoat, *Qualicoat Specifications 2021*, Qualicoat technical report, 2021.
60 F. E. M. O'Brien, *J. Sci. Instrum.*, 1948, **25**, 73–76.
61 E. Mysliu, O. Lunder and A. Erbe, *Data package for: Role of aluminium hydrides in localised corrosion of aluminium revealed by operando Raman spectroscopy*, BIRD, `https://hdl.handle.net/11250/3056964`, 2023.
62 P. P. Leblanc and G. S. Frankel, *J. Electrochem. Soc.*, 2004, **151**, B105.
63 D. Iqbal, R. S. Moirangthem, A. Bashir and A. Erbe, *Mater. Corros.*, 2014, **65**, 370–375.
64 F. Scholz, W. Unkrig, P. Eiden, M. A. Schmidt, A. Garsuch and I. Krossing, *Eur. J. Inorg. Chem.*, 2015, **2015**, 3128–3138.
65 C. Xu, S. Zhao, Y. Du, W. Zhang, P. Li, H. Jin, Y. Zhang, Z. Wang and J. Zhang, *ChemElectroChem*, 2019, **6**, 3350–3354.
66 I. R. Beattie, H. E. Blayden, S. M. Hall, S. N. Jenny and J. S. Ogden, *J. Chem. Soc., Dalton Trans.*, 1976, 666–676.
67 W. W. Rudolph, R. Mason and C. C. Pye, *Phys. Chem. Chem. Phys.*, 2000, **2**, 5030–5040.
68 H. Kanno, T. Yamaguchi and H. Ohtaki, *J. Phys. Chem.*, 1989, **93**, 1695–1697.
69 P. Thomas, V. Ramakrishnan and V. Vaidyan, *Thin Solid Films*, 1989, **170**, 35–40.
70 A. M. Ahern, P. R. Schwartz and L. A. Shaffer, *Appl. Spectrosc.*, 1992, **46**, 1412–1419.
71 T. Schram, J. D. Laet and H. Terryn, *J. Electrochem. Soc.*, 1998, **145**, 2733–2739.
72 M. Tkacz, T. Palasyuk, J. Graetz and S. Saxena, *J. Raman*

Spectrosc., 2008, **39**, 922–927.
73 T. Kato, Y. Nakamori, S. Orimo, C. Brown and C. Jensen, *J. Alloys Compd.*, 2007, **446-447**, 276–279.
74 Y. Wang, J.-A. Yan and M. Y. Chou, *Phys. Rev. B*, 2008, **77**, 014101.
75 J. L. White and S. L. Hem, *J. Pharm. Sci.*, 1975, **64**, 468–469.
76 C. J. Serna, J. L. White and S. L. Hem, *Soil Sci. Soc. Am. J.*, 1977, **41**, 1009–1013.
77 G. Melani, Y. Nagata, J. Wirth and P. Saalfrank, *J. Chem. Phys.*, 2018, **149**, 014707.
78 J. Y. Ying, J. B. Benziger and H. Gleiter, *Phys. Rev. B*, 1993, **48**, 1830–1836.
79 N. J. Cherepy, T. H. Shen, A. P. Esposito and T. M. Tillotson, *J. Colloid Interface Sci.*, 2005, **282**, 80–86.
80 H. D. Ruan, R. L. Frost and J. T. Kloprogge, *J. Raman Spectrosc.*, 2001, **32**, 745–750.
81 F. R. L. Faulstich, H. V. Castro, L. F. C. de Oliveira and R. Neumann, *Spectrochim. Acta A*, 2011, **80**, 102–105.
82 S. S. C. Pushparaj, N. D. Jensen, C. Forano, G. J. Rees, V. Prevot, J. V. Hanna, D. B. Ravnsbæk, M. Bjerring and U. G. Nielsen, *Inorg. Chem.*, 2016, **55**, 9306–9315.
83 A. Kiss, G. Keresztury and L. Farkas, *Spectrochim. Acta A*, 1980, **36**, 653–658.
84 A. Kreta, M. Rodošek, L. Slemenik Perše, B. Orel, M. Gaberščček and A. Šurca Vuk, *Corros. Sci.*, 2016, **104**, 290–309.
85 P. Tarte, *Spectrochim. Acta A*, 1967, **23**, 2127–2143.
86 J. Creus, A. Perez, C. Berziou, E. Conforto, F. Xavier, C. Rébéré, S. Cohendoz, S. Touzain, F. Sanchette and A. Billard, *NACE: Int. Corros. Conf. Ser.*, 2012, 1568.
87 C. Dyer, P. J. Hendra, W. Forsling and M. Ranheimer, *Spectrochim. Acta A*, 1993, **49**, 691–705.
88 P. Brüesch, R. Kötz, H. Neff and L. Pietronero, *Phys. Rev. B*, 1984, **29**, 4691–4696.
89 C. J. Serna, L. J. C., J. L. White and S. L. Hem, *J. Pharm. Sci.*, 1983, **72**, 769–771.
90 C. Li, J. Patra, J. Li, P. C. Rath, M.-H. Lin and J.-K. Chang, *Adv. Funct. Mater.*, 2020, **30**, 1909565.
91 H. Edwards, D. Farwell and A. Johnson, *J. Mol. Struct.*, 1995, **344**, 37–44.
92 S. Adhikari, J. Lee and K. R. Hebert, *J. Electrochem. Soc.*, 2008, **155**, C16.
93 S. Adhikari and K. R. Hebert, *J. Electrochem. Soc.*, 2008, **155**, C189.
94 G. G. Perrault, *J. Electrochem. Soc.*, 1979, **126**, 199–204.
95 Y. Yu and Y. Li, *Corros. Sci.*, 2020, **168**, 108568.
96 C. M. A. Brett, *J. Appl. Electrochem.*, 1990, **20**, 1000–1003.
97 J. Mol, B. Hinton, D. Van Der Weijde, J. De Wit and S. Van Der Zwaag, *Corros. Sci.*, 2000, **35**, 1629–1639.
98 A. Bautista, *Prog. Org. Coat.*, 1996, **28**, 49–58.
99 A. Almalla, O. Ozcan and J. Witt, *Adv. Eng. Mater.*, 2022, **24**, 2101342.
100 A. Afseth, J. Nordlien, G. Scamans and K. Nisancioglu, *Corros. Sci.*, 2002, **44**, 2529–2542.
101 R. Ambat, A. J. Davenport, G. M. Scamans and A. Afseth, *Corros. Sci.*, 2006, **48**, 3455–3471.
102 M. G. Strebl, M. P. Bruns, G. Schulze and S. Virtanen, *J. Electrochem. Soc.*, 2021, **168**, 011502.
103 E. C. Scholtz, J. R. Feldkamp, J. L. White and S. L. Hem, *J. Pharm. Sci.*, 1984, **73**, 967–973.
104 X. G. Zhang, *Corrosion and electrochemistry of zinc*, Plenum Press, New York, 1996.
105 P. Qiu, C. Leygraf and I. Odnevall Wallinder, *Mater. Chem. Phys.*, 2012, **133**, 419–428.
106 I. Wallinder, W. He, P.-E. Augustsson and C. Leygraf, *Corros. Sci.*, 1999, **41**, 2229–2249.
107 R. Szymanski, D. Jamieson, A. Hughes, A. Mol, S. van der Zwaag and C. Ryan, *Nucl. Instrum. Methods Phys. Res. B*, 2002, **190**, 365–369.
108 Y. Chen and A. Erbe, *Surf. Sci.*, 2013, **607**, 39–46.